

Impact of Semiconducting Perylene Diimide Nanoparticle Size on Lymph Node Mapping and Cancer Imaging

Zhen Yang,^{†,‡,||} Rui Tian,^{§,‡,||} Jinjun Wu,[†] Quli Fan,^{*,†} Bryant C. Yung,[‡] Gang Niu,[‡] Orit Jacobson,[‡] Zhantong Wang,[‡] Gang Liu,^{*,§} Guocan Yu,[‡] Wei Huang,[†] Jibin Song,^{*,‡} and Xiaoyuan Chen^{*,‡}

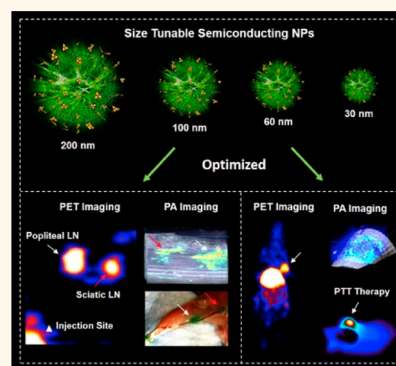
[†]Key Laboratory for Organic Electronics and Information Displays & Institute of Advanced Materials (IAM), Jiangsu National Synergetic Innovation Center for Advanced Materials (SICAM), Nanjing University of Posts & Telecommunications, Nanjing 210023, China

[‡]Laboratory of Molecular Imaging and Nanomedicine (LOMIN), National Institute of Biomedical Imaging and Bioengineering (NIBIB), National Institutes of Health (NIH) Bethesda, Maryland 20892, United States

[§]State Key Laboratory of Molecular Vaccinology and Molecular Diagnostics & Center for Molecular Imaging and Translational Medicine, School of Public Health, Xiamen University, Xiamen 361102, China

Supporting Information

ABSTRACT: Semiconducting molecules of perylene diimide (PDI) with strong light absorption properties in the near-infrared region and good biocompatibility have received increasing attention in the field of theranostics, especially as photoacoustic (PA) imaging agents. Herein, we report a series of [⁶⁴Cu]-labeled PDI nanoparticles (NPs) of different sizes (30, 60, 100, and 200 nm) as dual positron emission tomography (PET) and PA imaging probes and photothermal therapy agents. The precise size control of the PDI NPs can be achieved by adjusting the initial concentration of PDI molecules in the self-assembly process, and the photophysical property of different sized PDI NPs was studied in detail. Furthermore, we systematically investigated the size-dependent accumulation of the PDI NPs in the lymphatic system after local administration and in tumors after intravenous injection by PA and PET imaging. The results revealed that 100 nm is the best size for differentiating popliteal and sciatic LNs since the interval is around 60 min for the NPs to migrate from popliteal LNs to sciatic LNs, which is an ideal time window to facilitate surgical sentinel LN biopsy and pathological examination. Furthermore, different migration times of the different-sized PDI NPs will provide more choices for surgeons to map the specific tumor relevant LNs. PDI NP theranostics can also be applied to imaging-guided cancer therapy. The NPs with a size of 60 nm appear to be the best for tumor imaging and photothermal cancer therapy due to the maximum tumor accumulation efficiency. Thus, our study not only presents organic PDI NP theranostics but also introduces different-sized NPs for multiple bioapplications.



KEYWORDS: semiconducting nanoparticle, lymph node mapping, photoacoustic imaging, positron emission tomography imaging, photothermal therapy

The size of nanoparticles (NPs) has a dramatic effect on *in vivo* biodistribution, tumor accumulation, pharmacokinetics, therapeutic effect, *etc.*^{1–4} In cancer research, there has been a continuous effort to determine the best sized NPs to improve tumor diagnosis and treatment.^{5,6} For example, Chan *et al.* studied the size effect of PEGylated gold NPs (AuNPs) in tumor accumulation, relying on the enhanced permeability and retention (EPR) effect, and 60 nm AuNP appeared to be best suited for tumor passive targeting among 20–100 nm NPs.⁷ Shen *et al.* investigated the tumor accumulation and therapeutic effect of a series poly(prodrug) micelles with different sizes ranging from 30 to 200 nm.⁸ The results showed that the larger micelles had higher tumor

accumulation, but smaller micelles had higher penetration capacity in the tumor region and better therapeutic efficacy. Moreover, NP size can be of vital importance to imaging and treating central nervous system disorders. For example, Liu *et al.* used different sized 2,3-bis(4-(phenyl(4-(1,2,2-triphenylvinyl)phenyl)amino)phenyl)fumarionitrile (TPET-PAFN) NPs to evaluate blood–brain barrier (BBB) permeability and found that NPs with size greater than 30 nm do not

Received: February 22, 2017

Accepted: March 27, 2017

Published: March 27, 2017

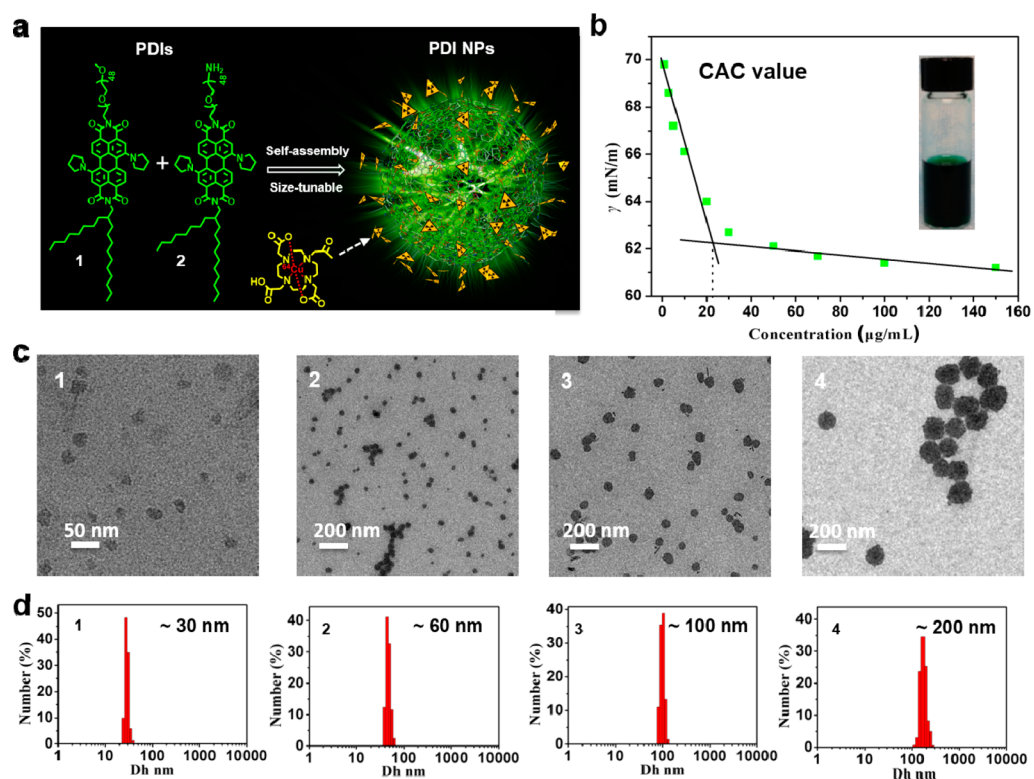


Figure 1. (a) Schematic and cartoon illustrations of the structures of PDI molecules and cartoon of size-tunable PDI NPs. (b) Surface tension of water as a function of the PDI concentration and the critical aggregation concentration (CAC) of PDIs is 22.5 mg/L in water. Inset: aqueous solution of PDI NPs. (c) TEM images and (d) dynamic light scattering results of different sized PDI NPs.

extravasate, while NPs of 10 nm could leak from nonischemic regions of the brain in a photothrombotic ischemia (PTI) model.⁹ The various observations of size-dependent effects of nanotheranostics manifest the need for careful study of the physicochemical properties of each type of NPs for their specific bioapplications.¹⁰

Sentinel lymph node (SLN) mapping and biopsy are standard of care procedures in the clinic for therapeutic decision-making guidance of various malignant tumors,^{11–13} such as breast cancer, gastric cancer, and prostate cancer.^{14–17} Accurate recognition of SLNs and differentiation from the second-echelon lymph nodes (LNs) could help surgeons improve the quality of pathological examination and refine the selection of LNs for surgical removal. For lymphatic system mapping, colloidal NPs with multimodality imaging capabilities are frequently used.^{15,18,19} Due to the wide size variance of the colloidal NPs, it is very challenging to match the surgery window with the NP migration and distribution. For colloidal nanoparticles used for LN imaging, the size is a critical factor which determines the rate of diffusion through the interstitium, draining in the lymphatic system, and uptake by the LNs.^{20,21} After interstitial injection, the colloidal NPs are cleared by lymphatic drainage with a speed that is inversely proportional to the particle size.²² To the best of our knowledge, there has rarely been a detailed study of using suitably labeled size-tunable NPs to control the migration for accurate SLN mapping.

Photoacoustic (PA) imaging provides deeper tissue penetration and higher spatial resolution than other commonly used methods, such as fluorescence optical imaging.^{23–30} PA imaging also allows portable detection and real-time imaging of SLNs during the surgery.^{31,32} Various semiconducting polymers and

oligomers with strong absorption in the near-infrared (NIR) region have been used for the detection of pH change in tumor,³³ oxidative environment recognition,³⁴ drug loading for cancer therapy,^{35,36} and so on. Herein, we report perylene diimide (PDI) derivatives with strong absorption in the NIR region as PA probes to detect orthotopic brain tumors in mice.³⁷

In this work, amphiphilic PDI derivatives were developed, which was further self-assembled into a series of PDI NPs with different sizes of 30, 60, 100, and 200 nm (Figure 1a). The relationship between the physical properties (absorption, PA, and photothermal properties) of the PDI NPs and their size was investigated in detail. The size-tunable PDI NPs were further labeled with radionuclide [⁶⁴Cu] for positron emission tomography (PET) imaging. Here, we systematically investigated the size-dependent accumulation effect of PDI NPs in the lymphatic system after local administration and in tumors after intravenous injection by using both PA and PET imaging approaches. The results revealed that 100 nm is the best size for differentiating popliteal and sciatic LNs since the interval is around 1 h for the migration of NPs from popliteal LNs to sciatic LNs. The nearly 1 h interval is sufficient for the surgeon to perform SLN biopsy and pathological examination to make decision for the following surgery. In addition, different migration times of the different sized NPs will provide more choices for surgeons to map the specific tumor relevant LNs. The intravenous injection results showed that the NPs with a diameter around 60 nm demonstrated the best properties for tumor imaging and photothermal cancer therapy due to the maximization of tumor accumulation efficiency.

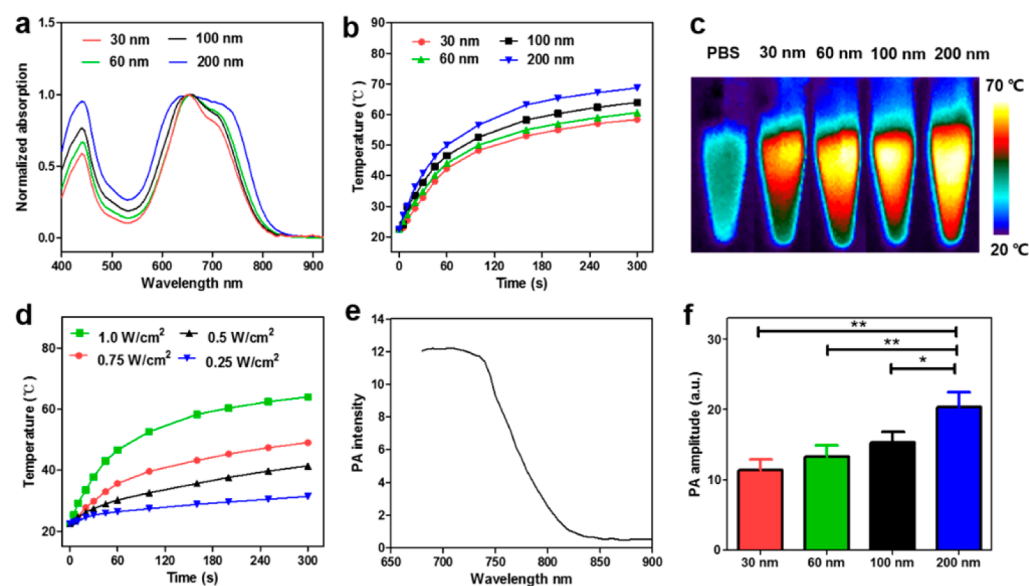


Figure 2. (a) Normalized UV–vis spectra of the different-sized PDI NPs in water. (b) Temperature variation of different-sized PDI NPs in aqueous solution as a function of laser irradiation time. (c) Infrared thermal images of different sized PDI NPs in aqueous solution and pure PBS irradiated with 675 nm laser at a power density of 1 W cm^{-2} for 300 s. (d) Photothermal profiles of PDI NPs in PBS upon laser irradiation at different power densities. (e) Representative PA spectra of PDI NPs in an *in vivo* phantom. (f) PA amplitudes of different sized PDI NPs at 680 nm at the same optical density. * $p < 0.05$ and ** $p < 0.01$.

RESULTS AND DISCUSSION

Preparation of Different-Sized PDI NPs. To prepare different-sized PDI NPs, we first synthesized two asymmetric amphiphilic PDI structures **1** and **2** as shown in Figure 1a. For structure **1**, the hydrophilic block is uncharged methoxy polyethylene glycol (mPEG₂₀₀₀), and the hydrophobic block is the PDI molecule and aliphatic chains, which provide an effective driving force for intermolecular aggregation in water where the flexible aliphatic chain contributes to uniform morphology during the self-assembly process. Compound **2** is structurally homologous to **1**, except that an amine group at the terminus is present to react with the macrocyclic chelator DOTA (tetraazacyclododecane-1,4,7,10-tetraacetic acid) for radiometal [⁶⁴Cu] labeling. DOTA chelator provides strong coordination with [⁶⁴Cu]. As shown in Figure S10, no free [⁶⁴Cu] was detected in the as-prepared [⁶⁴Cu]-labeled PDI NPs, suggesting the labeling efficiency was virtually 100%.

The detailed synthesis and characterizations of compound **1** and **2** are described in the Supporting Information (Scheme S1 and Figures S1–S9). When the mixture of **1** and **2** assembled in water at a ratio of 20:1, the water surface tension (γ) as a function of concentration was measured, yielding the CAC value of 22.5 mg/L (Figure 1b). The low CAC value facilitates self-assembly of the amphiphilic PDIs in aqueous solution and formation of uniform nanoparticles. PDI NP size can be precisely controlled from 30 to 200 nm by adjusting the initial concentration of the PDI molecules. For the preparation of different sized PDI NPs, we first dissolved PDIs **1** and **2** at a mass ratio of 20:1 into tetrahydrofuran (THF) at concentrations of 0.100, 2.00, 20.0, and 60.0 mg/mL, respectively, and then carefully added water into the above THF solutions. After slow and complete evaporation of THF, a series of uniform PDI NPs with sizes of 31.3 ± 3.2 , 62.3 ± 4.6 , 105.6 ± 13.4 , and 195.1 ± 18.6 nm were prepared. The uniform spherical nanostructures and narrow size distribution of the obtained PDI NPs were confirmed by TEM images and DLS results, as shown in Figure 1c,d. A small number of amine groups on the

NP surface can be used for coupling with DOTA, followed by [⁶⁴Cu] labeling for PET imaging. The surface charge of PDI NPs changed from positive to negative after being modified with DOTA. The zeta potential of 60 nm PDI NPs changed from +35.32 to -40.54 eV after DOTA coupling.

Photophysical Properties of Different-Sized PDI NPs.

As shown in the normalized UV–vis spectra of the different-sized PDI NPs in Figure 2a, the absorption peak at 700 nm became broader when the size of the PDI NPs increased from 30 to 200 nm. Meanwhile, both the H-aggregate band at ~ 650 nm and monomer band at ~ 700 nm showed greater red shift with an increase in PDI NP size. This phenomenon is consistent with previous reports about the different-sized aggregates of semiconducting molecules.^{38,39} The stability and biocompatibility of the PDI NPs were further studied *in vitro*. All PDI NPs showed great colloidal stability after incubation in mouse serum at 37 °C for 30 days at a high concentration of 20 mg/mL (Figure S11). The cell viability test indicated that all NPs had almost no toxicity toward NIH-3T3 cells up to 100 $\mu\text{g/mL}$ of PDI NPs (Figure S12), suggesting the excellent biocompatibility of the PDI NPs, which is favorable for a variety of biomedical applications.

The photothermal (PTT) properties of the different sized PDI NPs were further investigated by using a 675 nm laser. Four kinds of NP solutions with the same optical density (0.1) at 680 nm ($\text{OD}_{680 \text{ nm}}$) were irradiated by 675 nm laser for 300 s at a power density of 1 W cm^{-2} . The variation of temperature and thermal images of these solutions was monitored using an infrared thermal camera (Figure 2b,c). The results showed that the PTT effect of the NPs increased with increasing size. For example, the solutions of 200, 100, 60, and 30 nm PDI NPs and PBS were heated to 44, 37, 35, 32, and 23 °C at 300 s post-irradiation, respectively. The difference between infrared thermal images of the four kinds of NPs in the tubes after 300 s irradiation can be easily distinguished in Figure 2c. PDI NPs maintained their spherical morphologies after laser irradiation (Figure S13). We also found that the PTT effect

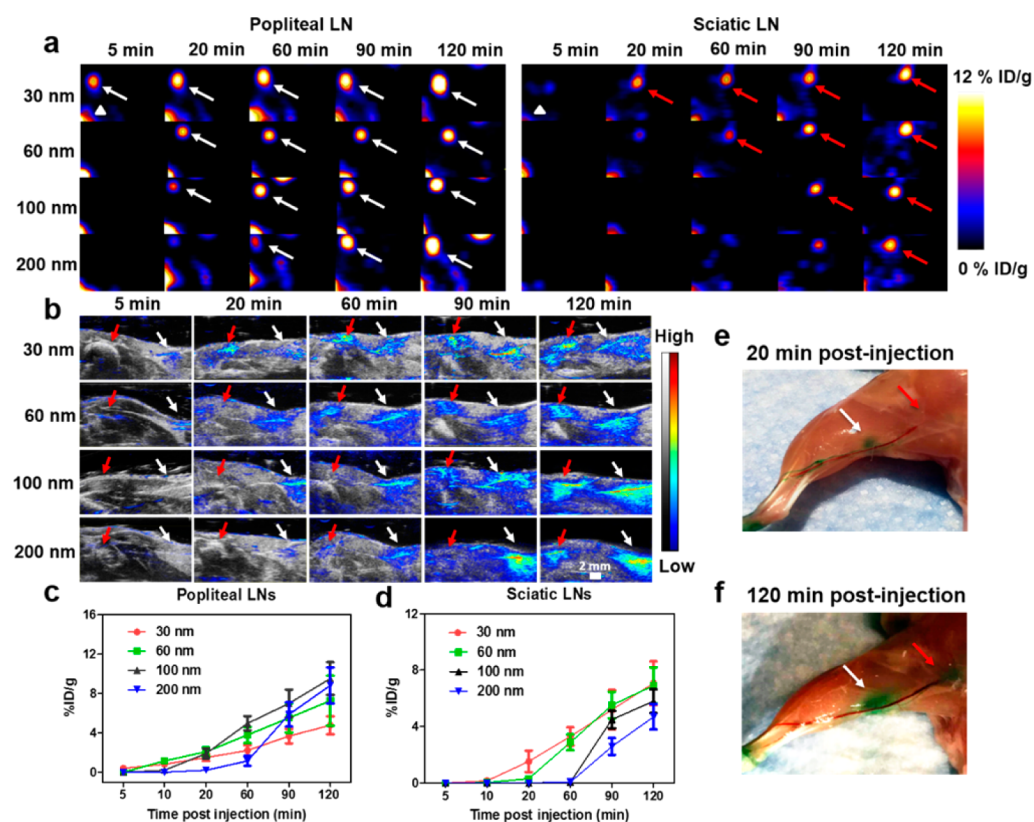


Figure 3. Representative (a) PET images and (b) overlaid coronal PA and ultrasound (US) images that show size-dependent uptake in popliteal lymph nodes (LNs) and sciatic LNs at different time points postinjection. Quantitative analysis of the total PDI NP PET signal with different size uptake in (c) popliteal LNs and (d) sciatic LNs. The LN mapping is visualized after footpad injection of PDI NPs at (e) 20 min and (f) 120 min postinjection. (All white arrows in figures represent popliteal LNs, red arrows represent sciatic LNs, and white arrowheads represent injection sites).

is relevant to the applied laser power density (Figure 2d). This interesting phenomenon, defined as enhanced thermal confinement effect,⁴⁰ arises from the fact that the generated heat is more difficult to diffuse to the outside with increased PDI NP size.

Many works have reported that the PA performance of nanomaterials is associated with their PTT property.²⁷ Thus, we further examined PA intensities of the different-sized NPs. Notably, the PA intensity of the PDI NPs also showed a size-dependent effect. The representative PA amplitude graph of PDI NPs showed that 680 nm is the optimal wavelength for PA imaging, as presented in Figure 2e. Under the same $OD_{680\text{ nm}}$ value, PA intensity increased with increasing size of the NPs, as shown in Figure 2f.

In Vivo PET and PA Lymphatic System Imaging by PDI NPs. The size-dependent migration of PDI NPs within the lymphatic system was investigated in a mouse model after local injection. The popliteal LN was proximal to the injection site, and the sciatic LN was located at a distal site. Small volume samples (25 μL containing 125 μg of PDI NPs for each mouse) were injected in the left rear footpad of FVB mice (3 mice/group), which were then allowed to move freely. The mice were anesthetized and the accumulation of PDI NPs was investigated by PET and PA imaging for up to 2 h. The use of PET and PA would be complementary and synergetic in clinical context because the superior sensitivity and depth of penetration of PET provides presurgical evaluation of the LNs, and the high spatial and temporal resolution of PA facilitates intraoperative identification of SLNs. To investigate

which size of PDI NPs is best for LN mapping, a series of PET images were first collected from different time points after injection of the four kinds of PDI NPs, respectively, as shown in Figure 3a.

At 5 min post injection, the popliteal LN was only visualized by 30 nm NPs, but no larger sized NPs were visualized within this time interval. At 20 min, both 60 and 100 nm NPs migrated to popliteal LNs, while 200 nm NPs did not arrive to the popliteal LN until 60 min post injection. Sciatic LNs were not visible at 5 min post injection with all sized NPs. The 30 and 60 nm NPs gradually accumulated in the sciatic LN 20 min post injection, while 100 and 200 nm NPs were still undetectable. At 90 min, the sciatic LN was already illuminated by 100 nm NPs, but 200 nm NPs were only starting to produce signal. At 120 min, 200 nm PDI NPs lights up the sciatic LN. The quantitative analysis of the PET signals in popliteal and sciatic LNs clearly verified the size-dependent migration and accumulation tendency of the four sized NPs. At 120 min, all LNs were illuminated from 30 to 200 nm. The uptakes of popliteal LN were 4.78 ± 0.92 , 7.26 ± 2.56 , 9.52 ± 1.65 , and $8.82 \pm 1.82\%$ ID/g, and sciatic LN were 7.08 ± 1.54 , 6.91 ± 1.27 , 5.8 ± 0.84 , $4.69 \pm 0.9\%$ ID/g, respectively (Figure 3c, d). Obviously, 30 and 60 nm NPs were not able to differentiate popliteal and sciatic LNs due to the short interval, and 100 and 200 nm NPs demonstrated better spatiotemporal resolution. This result also showed that 100 nm is the best size for recognizing popliteal and sciatic LNs because it takes 20 min to migrate to the popliteal LN and 90 min to the sciatic LN after injection of the samples (Figure S14). The nearly 1 h interval is

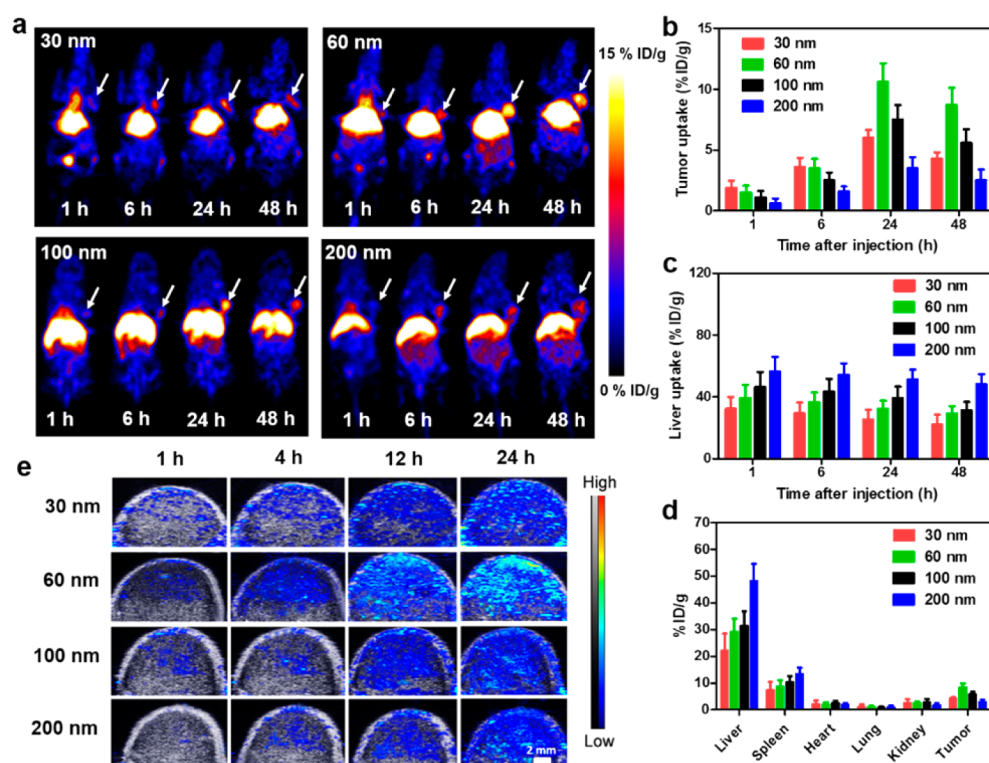


Figure 4. (a) Representative decay-corrected coronal small animal PET images acquired at 1, 6, 24, and 48 h after intravenous injection of different sized PDI NPs. White arrows represent U87MG tumors. (b) U87MG tumor and (c) liver uptake of different sized PDI NPs over time as quantified by PET scans at 1, 6, 24, and 48 h postinjection ($n = 3$ per group). (d) Biodistribution of the different sized PDI NPs in mice at 48 h post injection. (e) Overlaid coronal PA and US images of U87MG tumors acquired at 1, 4, 12, and 24 h after intravenous injection of different sized PDI NPs.

sufficient for the surgeon to perform SLN biopsy and pathological examination to make a decision for the following surgery.

As dual modality imaging agents, PDI NPs were further employed as PA imaging agents to investigate the size-dependent accumulation tendency of the NPs in LNs. Combining ultrasound (US) and PA imaging methods, the morphology of LNs was clearly delineated at each postinjection time point, as displayed in Figure 3b. Compared with PET images, more physiological information regarding popliteal LN and sciatic LN could be found in the overlaid US/PA images. From the PA images, the accumulation tendency of different-sized PDI NP was consistent with the PET imaging results, which also showed that 100 nm sized PDI NPs are most suitable for LN imaging. From PA images, the position and morphology of the LNs is clearly defined with high resolution. The strong and nonphotobleaching PA signal could favor monitoring LNs over a prolonged period for clinical applications. The quantitative region-of-interest (ROI) curves (Figures S15 and S16) quantitatively described the accumulation of the PDI NPs. From the 3D PA image of the LNs (Figure S17), the localization of the NPs in the popliteal and sciatic LNs was clearly observed at 20 and 90 min postinjection of the 100 nm PDI NPs. Furthermore, PDI NPs exhibit intense green color, which can be used for visual tracking during the surgery. At 20 and 120 min postinjection of 100 nm PDI NPs, the treated mice showed both their popliteal LN and sciatic LN sites in Figure 3e,f, respectively, which could be clearly distinguished by the apparent green color under bright field view.

In Vivo PET and PA Tumor Imaging by PDI NPs. To further explore the PDI NPs as a multifunctional theranostic agent, we studied the PDI NPs in cancer diagnosis and therapy. Herein, the tumor accumulation efficiency of these NPs in U87MG tumor model was investigated by dual PET and PA imaging approaches. PET imaging can provide a whole body scan to locate the tumor and quantify the size-dependent tumor accumulation of PDI NPs. Under PET imaging modality, four groups (three mice in each group) of mice were intravenously injected with the four kinds of different sized [^{64}Cu] labeled PDI NPs (200 μCi based on [^{64}Cu]), respectively, when the tumor size reached about 70 mm^3 . PET images of the mice in each group were scanned at multiple time points after injection. From the PET images of the mice at 24 h postinjection (Figure 4a), 60 nm PDI NPs showed higher PET signal in the tumor region than other sized PDI NPs. ROI analysis of the tumor and the liver uptake of these different sized PDI NPs were calculated. For tumor accumulation, PET intensity in the tumor region for each different sized NP gradually increased over 24 h postinjection, as shown in Figure 4b. The tumor accumulation of PDI NPs from 30 to 200 nm at 24 h postinjection were 6.04 ± 0.66 , 10.63 ± 1.54 , 7.51 ± 1.20 , and 3.50 ± 0.94 ID/g, respectively, whereas 60 nm NPs showed the best accumulation effect. Enhanced permeability and retention (EPR) effect is a result of abnormal porous blood capillaries and deficient lymphatic drainage, which is a nanoparticle size-dependent phenomenon. Thus, the particles with long blood circulation time and hence slow clearance from the body tend to have high tumor accumulation. The relatively high tumor uptake of 60 nm PDI NP is likely due to their longer circulation time and

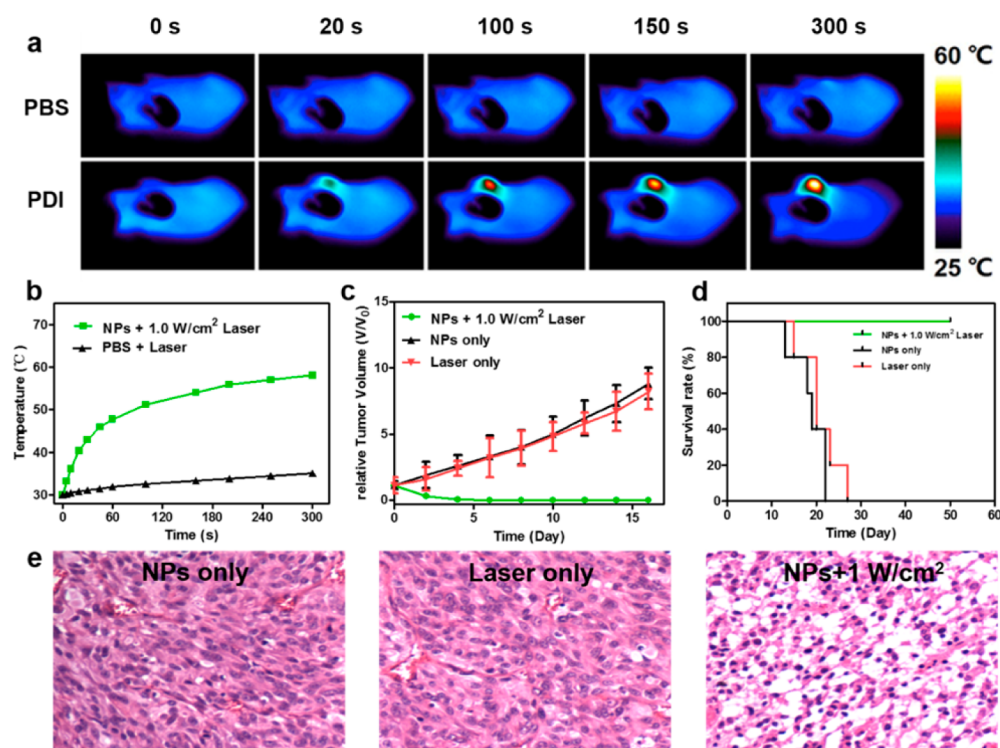


Figure 5. (a) Infrared thermal images of mice bearing U87MG tumors under 675 nm laser irradiation (1 W cm^{-2}) at 24 h postinjection of PBS or PDIs NPs. (b) Temperature changes of the tumor region treated with PDI NPs at 24 h postinjection and irradiated with 675 nm laser at a different power density of 1 W cm^{-2} . (c) Tumor growth curves and (d) survival curves of the mice after different treatments. (e) H&E-stained images of tumor sections collected from mice 1 day postirradiation.

lower liver accumulation than 100 and 200 nm NPs, and slower clearance than 30 nm NPs, as shown in Figure 4a–c.

The liver uptake results imply that larger sized NPs are more readily uptaken by the liver (Figure 4c). Figure 4d shows the *in vivo* biodistribution of the four kinds of PDI NPs at 48 h postinjection, observed in the liver ($22.00 \pm 6.51\%$, $29.22 \pm 4.92\%$, $31.33 \pm 5.50\%$, and $48.23 \pm 6.41\%$ ID/g), and the spleen ($7.22 \pm 3.23\%$, $8.54 \pm 2.56\%$, $10.23 \pm 2.23\%$, and $13.32 \pm 5.51\%$ ID/g). Uptake increased from 30 to 200 nm, indicating that the PDI NPs were mainly cleared through the mononuclear phagocyte system.

Encouraged by the excellent PA performance of PDI NPs, PA imaging was further employed to test the tumor accumulation efficiency of the four kinds of PDI NPs. In Figure 4e, we found that the PA signal in the tumor region was correspondingly increased over time after intravenous injection of the four kinds of PDI NPs into mice. Based on the results of average PA intensity (Figure S18) of the tumor at 24 h postinjection, the tumor accumulation efficiency of 60 nm NPs is higher than that of other sized NPs, which is consistent with the highest PA signal in the tumor region (Figure 4e). From the 3D PA image of the tumor (Figure S19), we can clearly see the morphology and calculate the size of the tumors, which is beneficial and essential for subsequent PA imaging-guided cancer therapy.

Imaging Guided Photothermal Cancer Therapy by PDI NPs. Encouraged by the high tumor accumulation efficiency, PTT therapy was further investigated with PDI NPs *in vivo*. Based on the PET and PA results, 60 nm PDI NPs were selected for treatment due to their high accumulation in tumor at 24 h postinjection. Figure 5a shows the remarkable temperature increase of the tumor after treatment with PDI

NPs under laser (675 nm) irradiation (1 W cm^{-2}) for 5 min, monitored by an infrared thermal camera. However, a negligible temperature increase in the tumor was observed in the mice treated with PBS. As presented in Figure 5b, the average temperature in the tumor region was increased with increasing irradiation time (1 W cm^{-2}). After irradiation, the tumor sizes and mice weight (Figure S20) were measured every 2 days after treatment. Remarkably, tumors treated with PDI NPs post laser irradiation were completely eliminated by day 10 post laser irradiation (Figure 5c), while mice in the other three control groups showed accelerated tumor progression and the survival curves (Figure 5d). In addition, hematoxylin and eosin (H&E)-stained images (Figure 5e) of tumor sections collected on 1 day postirradiation showed that the tumor cells treated with 1 W cm^{-2} were severely diminished. Conversely, all of the cells were healthy in the control groups. The above results suggest that 60 nm PDI NPs with excellent biocompatibility would be promising agents for imaging guided cancer therapy.

CONCLUSION

In conclusion, we have successfully developed a series of PDI NPs with different sizes of 30, 60, 100, and 200 nm, exhibiting excellent PA and PTT effects and serving as a dual PET and PA imaging probe and photothermal agent. The precise size control over the PDI NPs can be achieved by tuning the concentration of the initial concentration of PDI molecules in the self-assembly process. Extremely low CAC value and PEG protection facilitated the excellent stability and biocompatibility. By taking full advantage of these multifunctional PDI NPs, PA and PET imaging study revealed size-dependent LN and tumor accumulation effect. It was demonstrated that 100 nm PDI NPs are most suitable for LN mapping and 60 nm PDI

NPs are ideal for passive tumor targeting. Furthermore, this series of PDI NPs might have potential for other applications that were not explored in this study, such as using sub-30 nm PDI NPs to detect cerebrovascular diseases. Thus, our study not only presents organic semiconducting PDI NP theranostics but also proposes different sized NPs for multiple biomedical applications.

EXPERIMENTAL SECTION

Materials and Characterization. All solvents unless specified were obtained from Sigma-Aldrich and used as received. Synthesis routes and characterization of PDI molecule could be found in the [Supporting Information](#). Transmission electron microscopy (TEM) was conducted on a Jeol JEM 2010 electron microscope at an acceleration voltage of 300 kV. UV-vis absorption spectra were recorded by using a Shimadzu UV-2501 spectrophotometer. ^1H NMR spectra were obtained on a Bruker AV300 scanner using CDCl_3 as the solvent. Dynamic light scattering (DLS) was performed on a Malvern ZetaSizer Nano. PA spectra and PA/US coregistered images were acquired with a LAZR instrument (Visual Sonic Vevo 2100 LAZR Imaging System). PET imaging was performed using Inveon micro PET scanner (Siemens Medical Solutions).

Preparation of Different-Sized PDI NPs. PEG-based PDI 1 and 2 with a ratio of 20:1 were dissolved in 2 mL of THF with different concentrations. Deionized water (1 mL) was slowly dropped into the above solution with rapid stirring. THF was then removed by argon flow on the solution surface under stirring at 40 °C. A clear green aqueous solution was then obtained. The resultant products were stored at 4 °C for further use. The final PDI NPs were reconstituted in PBS and filtered through a 0.22 μm filter for the following cell and animal experiments. TEM and DLS data showed that the as-prepared PDI NPs are size tunable according to the PDI concentration in initial THF.

Photothermal Effect of Different-Sized PDI NPs. PDI NP solutions were irradiated along with 100 μL of a control PBS solution. The solutions were irradiated with a 675 nm laser at a power intensity of 1 W cm^{-2} for 5 min. A SC300 infrared camera was used to collect thermal images and quantify solution temperature.

Cell Viability. *In vitro* cytotoxicity of PDI NPs was determined in NIH-3T3 cells by the MTT assay. NIH-3T3 cells were incubated in a 96-well plate in DMEM medium containing 10% FBS and 1% penicillin/streptomycin at 37 °C in 5% CO_2 -humidified atmosphere for 24 h, and 5×10^3 cells were seeded per well. Cells were then cultured in the medium supplemented with indicated doses of PDI NPs with different sizes for 24 h. The final concentrations of NPs in the culture medium were fixed at 0.01, 0.1, 1, 10, and 100 $\mu\text{g/mL}$. Addition of 10 μL of MTT (0.5 mg/mL) solution to each well and incubation for 4 h at 37 °C was followed to produce formazan crystals. Then the supernatant was removed, and the products were lysed with 200 μL of DMSO. The absorbance value was recorded at 590 nm using a microplate reader. The absorbance of the untreated cells was used as a control, and its absorbance was used as the reference value for calculating 100% cellular viability.

PA Analysis of Phantoms. For studying the different PA properties with different-sized PDI NPs, a cuboid container was half filled with 1% agarose gel to half depth. Different-sized PDI NPs with the same optical density (OD_{680}) aqueous solutions were added to polyethylene 5 capillaries, and then the capillaries were laid on the surface of solidified agarose gel. The capillaries were further covered with thin 1% agarose gel to make the surface smooth.

Preparation of Radioactive [^{64}Cu]-Labeled Different-Sized PDI NPs. To prepare radiometal [^{64}Cu]-labeled PDI NPs, DOTA was conjugated on the PDI NP surface according to the reference procedure. Briefly, DOTA was activated by EDC and NHS at pH 5.5 for 30 min with a molar ratio of DOTA/EDC/NHS = 10:5:4. The activated DOTA was then reacted with amine based PDI NPs at a pH of 8.5. Then, the [^{64}Cu]-labeled PDI NPs were prepared by addition of [^{64}Cu] in 0.1 N sodium acetate (pH = 6.5) buffer, followed by incubation of the solution at 40 °C for 45 min. The resulting mixture

was purified using a PD-10 column with phosphate-buffered saline (PBS) as the mobile phase. The radioactive NPs with different sizes were collected for further experiments.

***In Vivo* Lymphatic System and Tumor PA and PET Imaging of Different Sized PDI NPs.** All animal experiments were approved by the animal care and use committee (ACUC) of the National Institutes of Health Clinical Center (NIHCC). For lymphatic system imaging, the FVB mice (3 mice/group) were used for local injection of left rear footpad with 25 μL containing 125 μg of different sized PDI NPs. PA and PET images with different sized PDI NPs were collected at various time points post injection.

For *in vivo* tumor imaging, U87MG tumor xenograft model was used. The U87MG tumor-bearing nude mice were prepared by inoculating cells (1×10^6 cells in 100 μL PBS) into the right shoulder of each mouse (female, 6 weeks old) under anesthesia, and the tumor was allowed to grow for about 15 days, until the volume was approximately 70 mm^3 . For *in vivo* PA imaging, the PDI NPs solution in PBS (200 μL , 5 mg/mL) was then injected intravenously into the tumor-bearing nude mice, and the tumor region of the mice was scanned with Visual Sonic Vevo 2100 LAZR system equipped with a 40 MHz, 256-element linear array transducer at different time points. For *in vivo* PET imaging, PDI NPs were labeled with radio-metal [^{64}Cu]. When the tumor size reached $\sim 70 \text{ mm}^3$, 200 μCi of [^{64}Cu] loaded onto different sized PDI NPs were intravenously tail injected into each tumor mouse. PET scans and image analysis were conducted using an Inveon micro PET scanner (Siemens Medical Solutions) at 1, 6, 24, and 48 h postinjection.

***In Vivo* Photothermal Cancer Therapy.** When the tumor volume was approximately 70 mm^3 (15 days after inoculation), 200 μL of 60 nm PDI NP solution with a concentration of 5 mg/mL was injected into mice under anesthesia ($n = 5/\text{group}$), respectively. At 24 h after the injection, the entire region of the tumor was irradiated with 675 nm laser at 1 W cm^{-2} for 5 min. During irradiation, real-time thermal images of the tumor region were acquired using a SC300 infrared camera. The average temperature in the tumor region was analyzed using FLIR analyzer professional software. After laser irradiation, a caliper was applied to measure the dimensions of the tumor at various time points. The tumor volume V (mm^3) at different days of postinjection was calculated using the formula $V = LW^2/2$, where L and W are the length and width of the U87MG tumor in millimeters, respectively.

ASSOCIATED CONTENT

Supporting Information

The Supporting Information is available free of charge on the ACS Publications website at DOI: 10.1021/acsnano.7b01261.

Synthesis scheme, ^1H and ^{13}C NMR, GPC, and MALDI-TOF mass of the PDI molecules and polymers, DLS, thermographic images, 3D PA LN and tumor images, and mice body weight changes (PDF)

AUTHOR INFORMATION

Corresponding Authors

*E-mail: iamqlfan@njupt.edu.cn.

*E-mail: gangliu.cmitm@xmu.edu.cn.

*E-mail: jibin.song@nih.gov.

*E-mail: shawn.chen@nih.gov.

ORCID

Zhen Yang: 0000-0003-4056-0347

Quli Fan: 0000-0002-9387-0165

Gang Liu: 0000-0003-2613-7286

Wei Huang: 0000-0001-7004-6408

Xiaoyuan Chen: 0000-0002-9622-0870

Author Contributions

\parallel Z.Y. and R.T. contributed equally to this work.

Notes

The authors declare no competing financial interest.

ACKNOWLEDGMENTS

This work was financially supported by the Intramural Research Program (IRP) of the NIBIB, NIH, the Arkansas Breast Cancer Research Program, the National Natural Science Foundation of China (Nos. 21674048, 21574064, and 61378081), and the Natural Science Foundation of Jiangsu Province of China (Nos. NY211003 and BM2012010), and Innovation Program for Ordinary Higher Education Graduate of Jiangsu Province of China (No. KYLX_0796).

REFERENCES

- (1) Chauhan, V. P.; Stylianopoulos, T.; Martin, J. D.; Popovic, Z.; Chen, O.; Kamoun, W. S.; Bawendi, M. G.; Fukumura, D.; Jain, R. K. Normalization of Tumour Blood Vessels Improves the Delivery of Nanomedicines in a Size-dependent Manner. *Nat. Nanotechnol.* **2012**, *7*, 383–388.
- (2) Jiang, W.; Kim, B. Y.; Rutka, J. T.; Chan, W. C. Nanoparticle-mediated Cellular Response is Size-dependent. *Nat. Nanotechnol.* **2008**, *3*, 145–150.
- (3) De Jong, W. H.; Hagens, W. I.; Krystek, P.; Burger, M. C.; Sips, A. J.; Geertsma, R. E. Particle Size-dependent Organ Distribution of Gold Nanoparticles after Intravenous Administration. *Biomaterials* **2008**, *29*, 1912–1919.
- (4) Tong, X.; Wang, Z.; Sun, X.; Song, J.; Jacobson, O.; Niu, G.; Kiesewetter, D. O.; Chen, X. Size Dependent Kinetics of Gold Nanorods in EPR Mediated Tumor Delivery. *Theranostics* **2016**, *6*, 2039–2051.
- (5) Guo, X.; Wei, X.; Jing, Y.; Zhou, S. Size Changeable Nanocarriers with Nuclear Targeting for Effectively Overcoming Multidrug Resistance in Cancer Therapy. *Adv. Mater.* **2015**, *27*, 6450–6456.
- (6) Sykes, E. A.; Chen, J.; Zheng, G.; Chan, W. C. W. Investigating the Impact of Nanoparticle Size on Active and Passive Tumor Targeting Efficiency. *ACS Nano* **2014**, *8*, 5696–5706.
- (7) Perrault, S. D.; Walkey, C.; Jennings, T.; Fischer, H. C.; Chan, W. C. W. Mediating Tumor Targeting Efficiency of Nanoparticles Through Design. *Nano Lett.* **2009**, *9*, 1909–1915.
- (8) Wang, J.; Mao, W.; Lock, L. L.; Tang, J.; Sui, M.; Sun, W.; Cui, H.; Xu, D.; Shen, Y. The Role of Micelle Size in Tumor Accumulation, Penetration, and Treatment. *ACS Nano* **2015**, *9*, 7195–7206.
- (9) Cai, X.; Bandla, A.; Mao, D.; Feng, G.; Qin, W.; Liao, L. D.; Thakor, N.; Tang, B. Z.; Liu, B. Biocompatible Red Fluorescent Organic Nanoparticles with Tunable Size and Aggregation-Induced Emission for Evaluation of Blood-Brain Barrier Damage. *Adv. Mater.* **2016**, *28*, 8760–8765.
- (10) Ling, D.; Lee, N.; Hyeon, T. Chemical Synthesis and Assembly of Uniformly Sized Iron Oxide Nanoparticles for Medical Applications. *Acc. Chem. Res.* **2015**, *48*, 1276–1285.
- (11) Porter, G. A.; Ross, M. I.; Berman, R. S.; Sumner, W. E., 3rd; Lee, J. E.; Mansfield, P. F.; Gershenwald, J. E. How Many Lymph Nodes are Enough During Sentinel Lymphadenectomy for Primary Melanoma? *Surgery* **2000**, *128*, 306–311.
- (12) Schrenk, P.; Rehberger, W.; Shamiyeh, A.; Wayand, W. Sentinel Node Biopsy for Breast Cancer: Does the Number of Sentinel Nodes Removed have an Impact on The Accuracy of Finding a Positive Node? *J. Surg. Oncol.* **2002**, *80*, 130–136.
- (13) Kuehn, T.; Bauerfeind, I.; Fehm, T.; Fleige, B.; Hausschild, M.; Helms, G.; Lebeau, A.; Liedtke, C.; Minckwitz, G. v.; Nekljudova, V.; Schmatloch, S.; Schrenk, P.; Staebler, A.; Untch, M. Sentinel-lymph-node Biopsy in Patients with Breast Cancer before and after Neoadjuvant Chemotherapy (SENTINA): a Prospective, Multicentre Cohort Study. *Lancet Oncol.* **2013**, *14*, 609–618.
- (14) Cai, X.; Liu, X.; Liao, L. D.; Bandla, A.; Ling, J. M.; Liu, Y. H.; Thakor, N.; Bazan, G. C.; Liu, B. Encapsulated Conjugated Oligomer Nanoparticles for Real-Time Photoacoustic Sentinel Lymph Node Imaging and Targeted Photothermal Therapy. *Small* **2016**, *12*, 4873–4880.
- (15) Rieffel, J.; Chen, F.; Kim, J.; Chen, G.; Shao, W.; Shao, S.; Chitgupi, U.; Hernandez, R.; Graves, S. A.; Nickles, R. J.; Prasad, P. N.; Kim, C.; Cai, W.; Lovell, J. F. Hexamodal Imaging with Porphyrin-phospholipid-coated Upconversion Nanoparticles. *Adv. Mater.* **2015**, *27*, 1785–1790.
- (16) Niu, G.; Chen, X. Lymphatic Imaging: Focus on Imaging Probes. *Theranostics* **2015**, *5*, 686–697.
- (17) Wang, Y.; Lang, L. X.; Huang, P.; Wang, Z.; Jacobson, O.; Kiesewetter, D. O.; Ali, I. U.; Teng, G. J.; Niu, G.; Chen, X. Y. *In Vivo* Albumin Labeling and Lymphatic Imaging. *Proc. Natl. Acad. Sci. U. S. A.* **2015**, *112*, 208–213.
- (18) Huang, X.; Zhang, F.; Lee, S.; Swierczewska, M.; Kiesewetter, D. O.; Lang, L.; Zhang, G.; Zhu, L.; Gao, H.; Choi, H. S.; Niu, G.; Chen, X. Long-term Multimodal Imaging of Tumor Draining Sentinel Lymph Nodes Using Mesoporous Silica-based Nanoprobes. *Biomaterials* **2012**, *33*, 4370–4378.
- (19) Antaris, A. L.; Chen, H.; Cheng, K.; Sun, Y.; Hong, G.; Qu, C.; Diao, S.; Deng, Z.; Hu, X.; Zhang, B.; Zhang, X.; Yaghi, O. K.; Alamparabil, Z. R.; Hong, X.; Cheng, Z.; Dai, H. A Small-molecule Dye for NIR-II Imaging. *Nat. Mater.* **2016**, *15*, 235–242.
- (20) Kumar, S.; Anselmo, A. C.; Banerjee, A.; Zakrewsky, M.; Mitragotri, S. Shape and Size-dependent Immune Response to Antigen-carrying Nanoparticles. *J. Controlled Release* **2015**, *220*, 141–148.
- (21) Reddy, S. T.; Rehor, A.; Schmoekel, H. G.; Hubbell, J. A.; Swartz, M. A. In vivo Targeting of Dendritic Cells in Lymph Nodes with Poly(propylene sulfide) Nanoparticles. *J. Controlled Release* **2006**, *112*, 26–34.
- (22) Mariani, G.; Moresco, L.; Viale, G.; Villa, G.; Bagnasco, M.; Canavese, G.; Buscombe, J.; Strauss, H. W.; Paganelli, G. Radioguided Sentinel Lymph Node Biopsy in Breast Cancer Surgery. *J. Nucl. Med.* **2001**, *42*, 1198–1215.
- (23) Lyu, Y.; Zhen, X.; Miao, Y.; Pu, K. Reaction-Based Semiconducting Polymer Nanoprobes for Photoacoustic Imaging of Protein Sulfenic Acids. *ACS Nano* **2017**, *11*, 358–367.
- (24) Lyu, Y.; Xie, C.; Chechetka, S. A.; Miyako, E.; Pu, K. Semiconducting Polymer Nanobiocjugates for Targeted Photothermal Activation of Neurons. *J. Am. Chem. Soc.* **2016**, *138*, 9049–9052.
- (25) Miao, Q.; Pu, K. Emerging Designs of Activatable Photoacoustic Probes for Molecular Imaging. *Bioconjugate Chem.* **2016**, *27*, 2808–2823.
- (26) Pu, K.; Shuhendler, A. J.; Jokerst, J. V.; Mei, J.; Gambhir, S. S.; Bao, Z.; Rao, J. Semiconducting Polymer Nanoparticles as Photoacoustic Molecular Imaging Probes in Living Mice. *Nat. Nanotechnol.* **2014**, *9*, 233–239.
- (27) Nie, L.; Chen, X. Structural and Functional Photoacoustic Molecular Tomography Aided by Emerging Contrast Agents. *Chem. Soc. Rev.* **2014**, *43*, 7132–7170.
- (28) Xu, M.; Wang, L. V. Photoacoustic Imaging in Biomedicine. *Rev. Sci. Instrum.* **2006**, *77*, 041101.
- (29) Troyan, S. L.; Kianzad, V.; Gibbs-Strauss, S. L.; Gioux, S.; Matsui, A.; Oketokoun, R.; Ngo, L.; Khamene, A.; Azar, F.; Frangioni, J. V. The FLARE Intraoperative Near-Infrared Fluorescence Imaging System: A First-in-Human Clinical Trial in Breast Cancer Sentinel Lymph Node Mapping. *Ann. Surg. Oncol.* **2009**, *16*, 2943–2952.
- (30) Lukianova-Hleb, E. Y.; Kim, Y.-S.; Belatsarkouski, I.; Gillenwater, A. M.; O'Neill, B. E.; Lapotko, D. O. Intraoperative Diagnostics and Elimination of Residual Microtumours with Plasmonic Nanobubbles. *Nat. Nanotechnol.* **2016**, *11*, 525–532.
- (31) Song, K. H.; Kim, C. H.; Cobley, C. M.; Xia, Y. N.; Wang, L. V. Near-Infrared Gold Nanocages as a New Class of Tracers for Photoacoustic Sentinel Lymph Node Mapping on a Rat Model. *Nano Lett.* **2009**, *9*, 183–188.
- (32) Erpelding, T. N.; Kim, C.; Pramanik, M.; Jankovic, L.; Maslov, K.; Guo, Z. J.; Margenthaler, J. A.; Pashley, M. D.; Wang, L. H. V.

Sentinel Lymph Nodes in the Rat: Noninvasive Photoacoustic and US Imaging with a Clinical US System. *Radiology* **2010**, *256*, 102–110.

(33) Miao, Q. Q.; Lyu, Y.; Ding, D.; Pu, K. Y. Semiconducting Oligomer Nanoparticles as an Activatable Photoacoustic Probe with Amplified Brightness for In Vivo Imaging of pH. *Adv. Mater.* **2016**, *28*, 3662–3668.

(34) Zhang, J.; Zhen, X.; Upputuri, P. K.; Pramanik, M.; Chen, P.; Pu, K. Activatable Photoacoustic Nanoprobes for In Vivo Ratiometric Imaging of Peroxynitrite. *Adv. Mater.* **2017**, *29*, 1604764.

(35) Song, J. B.; Yang, X. Y.; Jacobson, O.; Lin, L. S.; Huang, P.; Niu, G.; Ma, Q. J.; Chen, X. Y. Sequential Drug Release and Enhanced Photothermal and Photoacoustic Effect of Hybrid Reduced Graphene Oxide-Loaded Ultrasmall Gold Nanorod Vesicles for Cancer Therapy. *ACS Nano* **2015**, *9*, 9199–9209.

(36) Zhang, R.; Fan, Q.; Yang, M.; Cheng, K.; Lu, X.; Zhang, L.; Huang, W.; Cheng, Z. Engineering Melanin Nanoparticles as an Efficient Drug-Delivery System for Imaging-Guided Chemotherapy. *Adv. Mater.* **2015**, *27*, 5063–5069.

(37) Fan, Q. L.; Cheng, K.; Yang, Z.; Zhang, R. P.; Yang, M.; Hu, X.; Ma, X. W.; Bu, L. H.; Lu, X. M.; Xiong, X. X.; Huang, W.; Zhao, H.; Cheng, Z. Perylene-Diimide-Based Nanoparticles as Highly Efficient Photoacoustic Agents for Deep Brain Tumor Imaging in Living Mice. *Adv. Mater.* **2015**, *27*, 843–847.

(38) Wang, F.; Han, M. Y.; Mya, K. Y.; Wang, Y. B.; Lai, Y. H. Aggregation-driven Growth of Size-tunable Organic Nanoparticles Using Electronically Altered Conjugated Polymers. *J. Am. Chem. Soc.* **2005**, *127*, 10350–10355.

(39) Gorl, D.; Zhang, X.; Stepanenko, V.; Wurthner, F. Supramolecular Block Copolymers by Kinetically Controlled Co-self-assembly of Planar and Core-twisted Perylene Bisimides. *Nat. Commun.* **2015**, *6*, 7009.

(40) Aoki, H.; Nojiri, M.; Mukai, R.; Ito, S. Near-infrared Absorbing Polymer Nano-particle as a Sensitive Contrast Agent for Photoacoustic Imaging. *Nanoscale* **2015**, *7*, 337–343.